


Compound Twin Beams Without the Need of Genuine Photon-Number-Resolving Detection

Jan Peřina Jr. ^{1,*}, Antonín Černocho ¹ and Jan Soubusta ²

¹Joint Laboratory of Optics of Palacký University and Institute of Physics of the Czech Academy of Sciences, Faculty of Science, Palacký University, 17. listopadu 12, Olomouc 77146, Czech Republic

²Institute of Physics of the Czech Academy of Sciences, Joint Laboratory of Optics of Palacký University and Institute of Physics of CAS, 17. listopadu 50a, Olomouc 77207, Czech Republic

 (Received 25 February 2021; revised 25 May 2021; accepted 13 August 2021; published 31 August 2021)

A scheme for building stronger multimode twin beams from a greater number of identical twin beams sufficiently weak so that single-photon-sensitive *on-off* detectors suffice for their detection is studied. The statistical properties of these compound twin beams involving nonclassicality are analyzed for intensities up to hundreds of photon pairs. Their properties are compared with those of genuine twin beams that require photon-number-resolving detectors for their experimental investigation. The use of such compound twin beams for the generation of sub-Poissonian light and for the measurement of absorption with sub-shot-noise precision is analyzed. A suitable theoretical model for compound twin beams is developed to interpret the experimental data.

DOI: [10.1103/PhysRevApplied.16.024061](https://doi.org/10.1103/PhysRevApplied.16.024061)

I. INTRODUCTION

In the history of the detection of optical fields, two milestones occur. The first milestone was reached when solid-state light detectors became sensitive enough to recognize individual detected photons [due to the avalanche photodiodes (APDs) used [1]]. The second milestone is connected with the ability to count photons, which is a basic method for characterizing optical fields [2,3]. The first photon-number-resolving detectors (PNRDs) were simple: two single-photon counting modules were used to monitor the outputs of a balanced beam splitter and resolve up to two photons. More complex geometries were applied [4], including so-called fiber-loop PNRDs [5–7] with time multiplexing, to extend the range of detected photons. Spatial multiplexing, exploited in intensified CCD cameras [8,9] and silicon matrix photodetectors [10], considerably enlarged the range of detectable photon numbers. Finally, genuine PNRDs based on superconducting bolometers [11,12] were constructed. In such PNRDs, the number of detected photons is linearly proportional to the energy absorbed and is indirectly detected in superconducting metallic wires [13].

The use of PNRDs in the investigation of nonclassical properties of optical fields, including entangled fields, has revealed various states with unusual physical properties: states with reduced photon-number fluctuations (sub-Poissonian states [14], with Fock states as extreme

examples), states containing only odd or even photon numbers [15,16], and states with perfect correlations in the photon numbers [twin beams (TWBs)] [17], to name but a few. These states have found application in metrology (absolute detector calibration [18–21], quantum imaging [22,23], and sub-shot-noise measurements [24]). They have also been considered for use in quantum communications [25]. However, PNRDs at present are complex and expensive devices, and this limits the use of the above methods and applications.

This brings us to the question of whether PNRDs, with their capabilities to detect optical fields, can somehow be substituted by simpler APDs, with *on-off* detection, similarly to what is done in time-multiplexed and spatially multiplexed PNRDs. Such substitution is in principle possible for multimode optical fields that are composed of a greater number of spatial and spectral modes. When the mean numbers of photons in the individual modes are considerably lower than one, we may monitor the fields in individual modes with APDs. Provided that we are able to prepare the fields of individual modes independently, we can detect their properties with APDs mode by mode. Similarly, as the whole optical field is built from individual modes, its photon-number distribution is composed of contributions from APDs that monitor individual modes. Whereas such an approach is meaningless for the analysis of unknown optical fields, it has prospects for applications that use optical fields with well-defined properties, as mentioned above.

To demonstrate this approach, we consider TWBs and their application in quantum imaging. Several mean

*jan.perina.jr@upol.cz

photon pairs per imaged pixel are typically needed. The TWB used is typically composed of, say, N independent spatial modes, and its statistical operator $\hat{\varrho}$ is written as a product of statistical operators $\hat{\varrho}_j$ of individual modes:

$$\hat{\varrho} = \prod_{j=1}^N \hat{\varrho}_j. \quad (1)$$

In the TWB considered, the individual modes exhibit perfect photon pairing described by a thermal distribution with $b_{p,j}$ mean photon pairs,

$$\hat{\varrho}_j = \sum_{n_p=0}^{\infty} \frac{b_{p,j}^{n_p}}{(1 + b_{p,j})^{n_p+1}} |n_p\rangle_{s_j} \langle n_p|_{i_j} |n_p\rangle_{i_j} \langle n_p|_{s_j}, \quad (2)$$

and the Fock state $|n_p\rangle_{s_j}$ ($|n_p\rangle_{i_j}$) contains n_p photons in the signal (idler) field of mode j . The mean photon-pair numbers $b_{p,j}$ of the modes differ, but this has practically no influence on the properties exploited in the applications of TWBs. For this reason, we may substitute the TWB with statistical operator $\hat{\varrho}$ in Eq. (1) by a TWB composed of N equally populated individual modes. Such a TWB is described by the following statistical operator $\hat{\varrho}^c$:

$$\hat{\varrho}^c = \hat{\varrho}_{\text{av}}^{\oplus N}, \quad (3)$$

in which the statistical operator $\hat{\varrho}_{\text{av}}$ given by Eq. (2) contains $b_p = \sum_{j=1}^N b_{p,j}/N$ mean photon pairs. The TWB with statistical operator $\hat{\varrho}^c$ in Eq. (3) is then suitable for a practical realization in which we prepare a field with statistical operator $\hat{\varrho}_{\text{av}}$ N times. Thus, instead of measuring the stronger TWB given in Eq. (1) with two PNRDs, we measure N times a weak TWB with statistical operator $\hat{\varrho}_{\text{av}}$ with two APDs and sum the results to arrive at results appropriate to the TWB given in Eq. (3). We call such TWBs compound TWBs. The detection scheme is illustrated in Fig. 1, considering one of the beams that compose the TWB. We note that a similar scheme was applied in the experimental study of non-Gaussian states in Ref. [26].

The compound TWBs generated in the substitution scheme are interesting on their own. Here, we demonstrate their usefulness when we study the behavior of TWB nonclassicality for intensities varying by 3 orders of magnitude. The substitution scheme assures close similarity of the parameters of compound TWBs that differ in their intensities by orders of magnitude. Such an analysis would not be possible for the usual experimental TWBs.

Sub-shot-noise imaging and quantum metrology represent the most important applications of stronger TWBs (composed of several to several hundreds of photon pairs) at present. In one of their variants, they use sub-Poissonian fields as light sources for monitoring the absorption coefficients of samples. They rely on the fact that the fluctuations

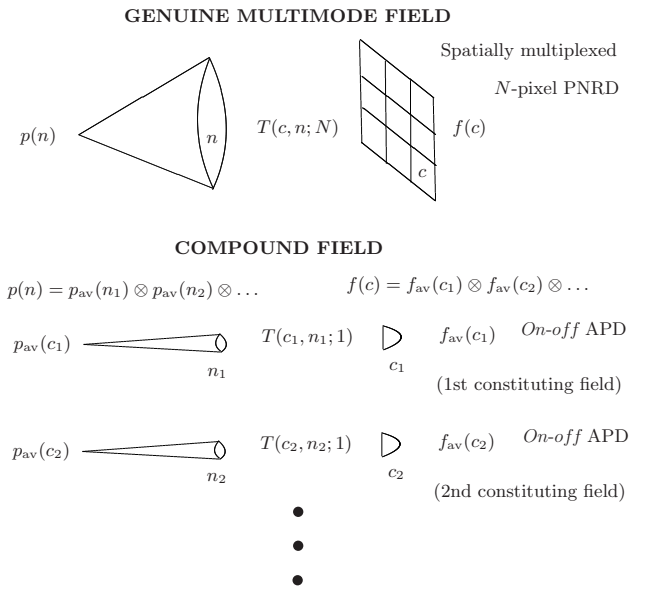


FIG. 1. Substitution scheme for a stronger multimode field with a photon-number distribution $p(n)$ detected by an N -pixel spatially multiplexed PNRD, giving a photocount histogram $f(c)$. The stronger field is replaced by N identical weak fields with photon-number distributions $p_{\text{av}}(n)$, detected by APDs that provide photocount histograms $f_{\text{av}}(c)$. The photon-number distribution $p(n)$ and photocount histogram $f(c)$ are obtained from the photon-number distributions $p_{\text{av}}(n)$ and photocount histograms $f_{\text{av}}(c)$ by N -fold convolution. The elements of the detection matrix $T(c, n; N)$ give the probabilities of detecting c photocounts out of n impinging photons with an N -pixel detector.

in photon numbers in such fields are suppressed below the shot-noise limit, which allows one to achieve better measurement precision. Postselection from a TWB [14,27–29], one arm of which is monitored with a PNRD, is one of the most efficient methods of sub-Poissonian-light generation. Using the above-discussed similarity of the parameters of compound TWBs, we investigate the nonclassicality of sub-Poissonian fields originating from compound TWBs depending on the intensity of the fields.

Finally, as a third example of the use of compound TWBs, we directly analyze the performance of compound TWBs in sub-shot-noise measurements [22,24,30,31] by determining the precision of absorption measurements depending on the compound-TWB intensity. Such measurements were recently applied in microscopy [32,33] and spectroscopy [34].

We note that the use of APDs instead of genuine PNRDs in the substitution scheme discussed here also benefits from the considerably higher absolute detection efficiencies of APDs.

The paper is organized as follows. Photon-number and photocount distributions of genuine and compound TWBs are introduced in Sec. II. In Sec. III, the experiment is described and analyzed, and the main characteristics of the

generated fields are given. The determination of the effective detection efficiency, which is an important parameter of PNRDs, is discussed in Sec. IV. Nonclassicality of compound TWBs is analyzed in Sec. V using suitable nonclassicality identifiers and the accompanying nonclassicality depths. The generation of sub-Poissonian light by postselection from compound TWBs is discussed in Sec. VI. Sub-shot-noise measurements of absorption coefficients using compound TWBs are investigated in Sec. VII. Conclusions are drawn in Sec. VIII. In the Appendix, a model for describing the correlations in the intra-pump-pulse intensity fluctuations is developed.

II. PHOTON-NUMBER AND PHOTOCOUNT DISTRIBUTIONS OF GENUINE AND COMPOUND TWIN BEAMS

The joint photon-number distribution $p_{si}(n_s, n_i)$ of an arbitrary TWB generated from parametric down-conversion can be described as a twofold convolution of three photon-number distributions p_p , p_s , and p_i belonging in turn to the paired, noise-signal, and noise-idler components of the TWB described here [35]:

$$p_{si}(n_s, n_i) = \sum_{n=0}^{\min(n_s, n_i)} p_s(n_s - n) p_i(n_i - n) p_p(n), \quad (4)$$

where n_s (n_i) gives the number of signal (idler) photons. In the model, we assume that the photon-number distributions of the components constituting the TWB are in the form of a multimode thermal Mandel-Rice distribution [3] that is derived for a field with M_a equally populated modes and a mean photon (or photon-pair) number B_a per mode:

$$p_a(n; M_a, B_a) = \frac{\Gamma(n + M_a)}{n! \Gamma(M_a)} \frac{B_a^n}{(1 + B_a)^{n+M_a}}, \quad a = s, i, p, \quad (5)$$

where Γ denotes the Γ function.

The joint photocount distribution $f_{si}(c_s, c_i)$ [3] registered by two PNRDs composed of N_s and N_i equally illuminated pixels with *on-off* detection for the field with photon-number distribution $p_{si}(n_s, n_i)$ given in Eq. (4) is given as follows:

$$f_{si}(c_s, c_i) = \sum_{n_s, n_i=0}^{\infty} T_s(c_s, n_s; N_s) T_i(c_i, n_i; N_i) p_{si}(n_s, n_i), \quad (6)$$

where c_s (c_i) denotes the number of signal (idler) photocounts, which refers to the photoelectrons registered by a detector after the absorption of photons.

For a detector with a quantum detection efficiency η_a , number of pixels N_a , and mean dark-count number per pixel D_a , the elements of the detection matrices

T_a , $a = s, i$, introduced in Eq. (6) are derived in the following form [9]:

$$T_a(c_a, n_a; N_a) = \binom{N_a}{c_a} (1 - D_a)^{N_a} (1 - \eta_a)^{n_a} (-1)^{c_a} \times \sum_{l=0}^{c_a} \binom{c_a}{l} \frac{(-1)^l}{(1 - D_a)^l} \left(1 + \frac{l}{N_a} \frac{\eta_a}{1 - \eta_a} \right)^{n_a}. \quad (7)$$

The derivation of Eq. (7) shows that when the mean number of photons illuminating one pixel is much less than one, i.e., when we can neglect illumination of a pixel by more than one photon, the elements of the detection matrix $T_a(c_a, n_a; N_a)$ in Eq. (7) can be written as being composed of the elements of independent detection matrices $T_a(c_a, n_a; 1)$ characterizing detection by individual pixels.

In the substitution scheme, we assume that a genuine stronger TWB is replaced by a compound TWB, i.e., an ensemble of N identical constituting TWBs detected by *on-off* APDs such that the mean photon numbers of the genuine and compound TWBs are the same. Although the mean photon-pair numbers of the constituting TWBs are much less than one, we still have to consider their multimode structure (see the discussion below). Provided that we have m_a modes in a constituting TWB, the mean photon (or photon-pair) numbers b_a per mode of a constituting TWB are given by $b_a = B_a M_a / (m_a N)$, $a = s, i, p$. A formula analogous to that in Eq. (4) gives us the corresponding joint signal-idler photon-number distribution $p_{si}^w(n_s, n_i)$ of a constituting TWB. The constituting TWBs are detected by two APDs, whose operation is described by the elements of the detection matrix T_a in Eq. (7) assuming $N_a = 1$, $a = s, i$. The joint photocount distribution $f_{si}^w(c_s, c_i)$ appropriate to one constituting TWB is given by

$$f_{si}^w(c_s, c_i) = \sum_{n_s, n_i=0}^{\infty} T_s(c_s, n_s; 1) T_i(c_i, n_i; 1) p_{si}^w(n_s, n_i). \quad (8)$$

For a compound TWB formed by N constituting TWBs, the probability f_{si}^c of having c_s signal photocounts together with c_i idler photocounts is determined by the following multiple convolution:

$$f_{si}^c(c_s, c_i; N) = \sum_{c_s, 1, c_{i,1}=0}^1 \cdots \sum_{c_s, N, c_{i,N}=0}^1 \delta_{c_s, \sum_{j=1}^N c_{s,j}} \delta_{c_i, \sum_{j=1}^N c_{i,j}} \times \prod_{j=1}^N f_{si}^w(c_{s,j}, c_{i,j}), \quad (9)$$

in which δ stands for the Kronecker symbol.

In analogy to Eqs. (8) and (9), the probability $p_{c_i}^w(n_i; c_s)$ of having n_i idler photons conditioned by the detection of

c_s signal photocounts in a constituting TWB is given as follows:

$$p_{c,i}^w(n_i; c_s) = \sum_{n_s=0}^{\infty} T_s(c_s, n_s; 1) p_{si}^w(n_s, n_i). \quad (10)$$

The conditional probability $p_{c,i}^c(n_i; c_s)$ of having n_i idler photons after detecting c_s signal photocounts in a compound TWB formed by N constituting TWBs is then expressed as

$$p_{c,i}^c(n_i; c_s, N) = \sum_{c_{s,1}=0}^1 \cdots \sum_{c_{s,N}=0}^1 \delta_{c_s, \sum_{j=1}^N c_{s,j}} \sum_{n_{i,1}=0}^{n_i} \cdots \sum_{n_{i,N}=0}^{n_i} \times \delta_{n_i, \sum_{j=1}^N n_{i,j}} \prod_{j=1}^N p_{c,i}^w(n_{i,j}; c_{s,j}). \quad (11)$$

III. EXPERIMENTAL CHARACTERIZATION OF COMPOUND TWIN BEAMS

The properties of compound TWBs are experimentally investigated in the setup shown in Fig. 2. The process of type-I parametric down-conversion in a LiIO_3 nonlinear crystal pumped by the third harmonic of a Nd-YAG laser at 355 nm and a repetition rate of 2.5 kHz is used

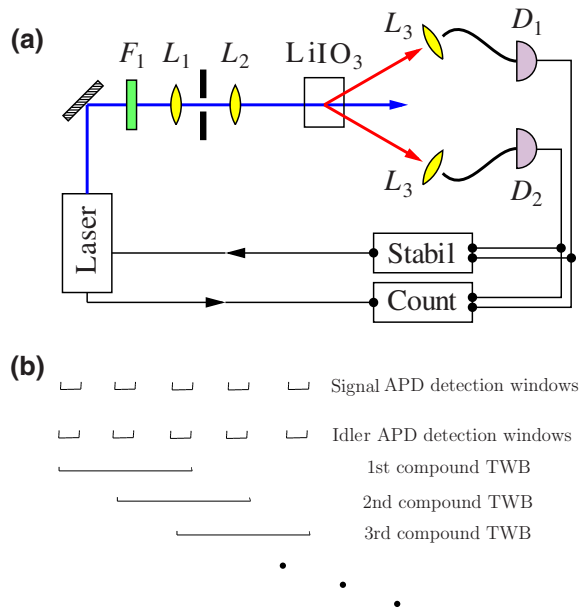


FIG. 2. (a) Experimental setup for generation of photon pairs in a nonlinear LiIO_3 crystal by short optical pulses, and their detection by single-photon APDs D_1 and D_2 ; a frequency filter F_1 and lenses $L_{1,2,3}$ transform the beams used. More details are given in the text. (b) Signal-APD and idler-APD detection windows and their grouping into triplets, which give measurements on compound TWBs formed by three constituting TWBs.

to generate photon pairs with degenerate photon wavelengths centered at 710 nm. The laser is kept closely above the threshold to give a power of only a few milliwatts. The third harmonic is spectrally cleaned with dichroic mirrors and a 10-nm-wide spectral filter. To obtain a pump beam with an acceptable spatial profile in the nonlinear crystal, we perform spatial filtering with a $4f$ system composed of two lenses (L_1, L_2) with focal lengths of 20 and 50 mm and a 50- μm -wide round aperture. The signal and idler photons are detected by single-photon APDs (Count-NIR from Laser Components) with nominal detection efficiencies of about 80% and very low dark count rates (less than 50 Hz). Before being detected, the photons are spatially filtered by coupling into multimode fibers by means of lenses L_3 (focal length 15.3 mm, clear aperture 5 mm). The electronic signals from the detectors are recorded simultaneously with a trigger from the laser using counting-logic electronics and sent directly to a computer for recording. The duration of the pump pulses is 6.5 ns, and, similarly, the signal and idler photons are emitted simultaneously in 6.5-ns-long time windows. The time delay between successive pulses is 4 ms. The detection events are recorded continuously and form two synchronized sequences of *on-off* detections (in the signal and idler beams). The laser power is stabilized with a feedback loop to maintain stable operation of the experiment over tens of hours. Feedback is provided by monitoring the average single-photon detection rate during the measurement: whenever the detection rate changes by more than 5%, the laser pump power is adjusted to compensate for this deviation.

The experimental data analyzed represent a sequence of 695×10^6 measurements by single-photon APDs in individual detection windows (triggered by individual pump pulses), with the following four possible outcomes: no detection in either the signal or the idler detector, detection only in the signal detector, detection only in the idler detector, or coincidence detection in both detectors. An outcome in each detection window represents a measurement on one constituting TWB. Grouping of the outcomes in neighboring detection windows then gives us information about compound TWBs. We group the detections in N successive detection windows to arrive at an experimental photocount histogram $f_{si}^c(c_s, c_i; N)$ characterizing a compound TWB formed by N constituting TWBs. When we form the photocount histograms of compound TWBs, the outcomes in the individual detection windows are used multiply, following the scheme presented in Fig. 2(b).

The joint signal-idler photon-number distribution $p_{si}^c(n_s, n_i; N)$ of a compound TWB formed by N constituting TWBs is then revealed using a reconstruction method based on the maximum-likelihood (ML) approach [36,37]. This gives us the following iteration procedure for the reconstructed photon-number distribution p_{si}^c (where j

stands for the iteration index):

$$\begin{aligned}
 & p_{si}^{c^{(j+1)}}(n_s, n_i; N) \\
 &= \sum_{c_s, c_i=0}^{\infty} F_{si}^{(j)}(c_s, c_i; N) T_s(c_s, n_s; N) T_i(c_i, n_i; N), \\
 & F_{si}^{(j)}(c_s, c_i; N) \\
 &= f_{si}^c(c_s, c_i; N) \left[\sum_{n'_s, n'_i=0}^{\infty} T_s(c_s, n'_s; N) T_i(c_i, n'_i; N) \right. \\
 & \quad \left. \times p_{si}^{c^{(j)}}(n'_s, n'_i; N) \right]^{-1}, \quad j = 0, 1, \dots \quad (12)
 \end{aligned}$$

We characterize the compound TWBs obtained by their photocount (photon-number) moments $\langle c_s^k c_i^l \rangle$ ($\langle n_s^k n_i^l \rangle$) determined from the formula

$$\langle c_s^k c_i^l \rangle = \sum_{c_s, c_i=0}^N c_s^k c_i^l f_{si}^{c^k c^l}(c_s, c_i; N). \quad (13)$$

The Fano factors $F_{c,a}$ ($F_{n,a}$), together with mean photocount (photon) numbers $\langle c_a \rangle$ ($\langle n_a \rangle$), $a = s, i$, defined in Eq. (13) are used to characterize the signal and idler marginal distributions:

$$F_{c,a} = \frac{\langle (\Delta c_a)^2 \rangle}{\langle c_a \rangle}, \quad (14)$$

where $\Delta c_a \equiv c_a - \langle c_a \rangle$. On the other hand, the noise-reduction-parameter R_c (R_n) and covariance C_c (C_n) of the photocount (photon) numbers c_s and c_i (n_s and n_i) are applied to quantify both the quantum and the classical correlations between the signal and idler fields:

$$R_c = \frac{\langle [\Delta(c_s - c_i)]^2 \rangle}{\langle c_s \rangle + \langle c_i \rangle}, \quad (15)$$

$$C_c = \frac{\langle c_s c_i \rangle}{\sqrt{\langle c_s^2 \rangle \langle c_i^2 \rangle}}. \quad (16)$$

The mean photocount numbers $\langle c_a \rangle$ and the corresponding mean photon numbers $\langle n_a \rangle$, $a = s, i$, of the marginal signal and idler fields of the compound experimental TWBs naturally increase linearly with the number N of constituting TWBs given by the number of grouped detection windows, as documented in Fig. 3(a). The Fano factors $F_{c,a}$ of the marginal experimental photocount histograms attain values slightly smaller than 1 [for the idler Fano factor $F_{c,i}$, see Fig. 3(b)]. The values of the

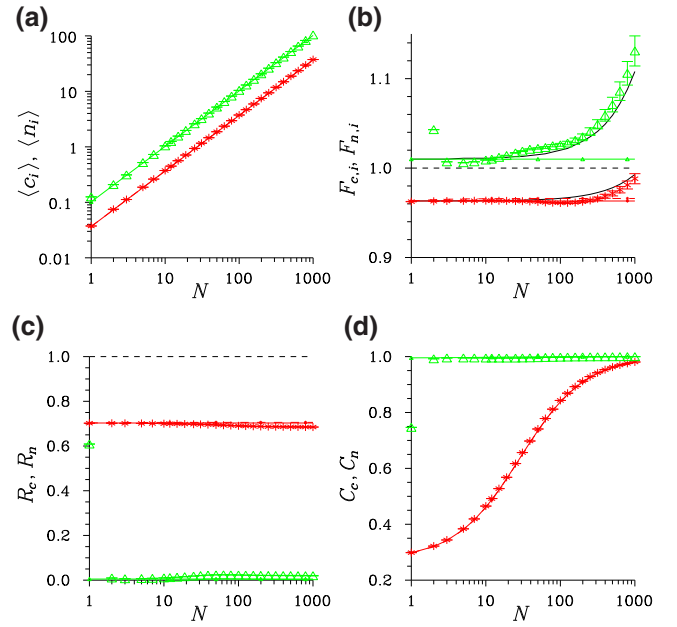


FIG. 3. (a) Mean number of photons $\langle n_i \rangle$ (photocounts $\langle c_i \rangle$) and (b) Fano factor $F_{n,i}$ ($F_{c,i}$) of the idler field, (c) noise-reduction parameter R_n (R_c), and (d) covariance C_n (C_c) of the compound TWBs, depending on the number N of grouped detection windows. Isolated symbols with error bars [in (a),(c),(d) they are smaller than the plotted symbols] are drawn for the experimental photocount histograms (red asterisks) and the fields reconstructed by the ML approach (green triangles). The solid (dashed) curves with symbols originate from the model of compound (genuine) TWBs detected by APDs (N -pixel PNRDs). The black plain solid curves are drawn for the model of compound TWBs with correlations in intra-pump-pulse intensity fluctuations. In (a),(c),(d), the red solid and dashed curves nearly coincide. The horizontal plain dashed lines indicate the border between the classical and nonclassical regions ($F = 1$, $R = 1$).

Fano factors $F_{c,a}$, $a = s, i$, of the detected photocount histograms smaller than 1 originate from the pileup effect [9,10]. This effect occurs in detection with a single-photon APD, which allows one to register up to one photocount. As the elements of the detection matrix in Eq. (7) incorporate this effect, any reconstruction that uses these elements corrects for the pileup effect. This is demonstrated in Fig. 3(b), where the values of the idler photon Fano factor $F_{n,i}$ are greater than 1, in agreement with the classical character of the marginal fields of compound TWBs. The photon Fano factors F_n of the marginal fields reconstructed by the ML approach increase systematically with an increasing number N of grouped detection windows. This behavior is observed also for the Fano factors F_c characterizing the photocount histograms, especially for larger numbers N of grouped detection windows [Fig. 3(b)]. This increase is caused by weak temporal instability of the pump-pulse intensities, which manifests

itself as correlations in the intra-pump-pulse intensity fluctuations. A stochastic model that describes this effect is developed in the Appendix.

We compare the quantities characterizing both the experimental photocount histograms $f_{si}^c(c_s, c_i; N)$ and the photon-number distributions $p_{si}^c(n_s, n_i; N)$ reconstructed by the ML approach with the predictions of two basic models. In the first model of a compound TWB, we assume that each detection window, monitored by two APDs (one in the signal beam, the other in the idler beam), is illuminated by a Gaussian constituting TWB with $m_p = m_s = m_i = 10$ modes and with mean photon (or photon-pair) numbers per mode $b_p = 1.0185 \times 10^{-2}$, $b_s = 8 \times 10^{-5}$, and $b_i = 2 \times 10^{-5}$. We make the assumption $m_p = m_s = m_i$ for the numbers of modes in the (typical) constituting TWB and estimate the number m_p of modes in the dominant paired component of the constituting TWB from the reconstructed Fano factors F_{n_s} and F_{n_i} . The mean photon (or photon-pair) numbers b_p , b_s , and b_i are then set to accord with the mean photon numbers $\langle n_s \rangle$ and $\langle n_i \rangle$ of the constituting TWB reconstructed by the ML approach. We note that the constituting TWB is practically noiseless (the unpaired noise photons comprise less than 1% of the intensity of the constituting TWB). The second model is simpler. It assumes a genuine strong TWB having $M_a = Nm_a$ modes each containing b_a mean photons or photon pairs, $a = p, s, i$, and being monitored by two genuine PNRDs resolving up to N photons (N -pixel PNRDs).

The simpler second model, of a genuine TWB detected by two N -pixel PNRDs with the photon-number distribution $p_{si}(n_s, n_i)$ given in Eq. (4), predicts that the Fano factors F_n and F_c are independent of the number N of detection pixels (windows) [see the dashed curves in Fig. 3(b)]. We arrive at nearly constant values of the photocount Fano factors F_c also when we apply the more elaborated first model of a compound TWB, whose constituting TWBs are detected by APDs. The model is described by Eq. (9), which gives the solid curves in Fig. 3(b). The difference between the two models is the following. In the case of a genuine TWB and N -pixel PNRDs, each photon, independently of the mode in which it resides, can be detected by any pixel. This contrasts with the case of a compound TWB detected by APDs, in which photons from the k th constituting TWB can be detected only in the k th detection window of the APDs used ($k = 1, \dots, N$). Thus, whereas the pileup effect does not change with an increasing number N of detection windows of the APDs in the case of a compound TWB, it weakens with an increasing number N of detection pixels of the PNRDs in the case of a genuine TWB. Reduction of the pileup effect in the latter case then results in a small increase in the artificially low values of the photocount Fano factors F_c with an increasing number N of pixels [see the dashed curve in Fig. 3(b)].

A comparison of the results of the two models with the measured and reconstructed values of the Fano factors F_c

and F_n in Fig. 3(b) reveals the relatively strong influence of the above-mentioned correlations in the intra-pump-pulse intensity fluctuations. The corresponding model presented in the Appendix, which represents a suitable generalization of the first model, provides the solid plain curves in Fig. 3(b), which are in good agreement with the measured values. According to the model in the Appendix, the greater the number N of grouped detection windows is, the greater the values of the Fano factors F are. However, as the correlations in the intra-pump-pulse intensity fluctuations are specific to our experimental setup, we refer to the model in the Appendix only when needed.

On the other hand, the correlations quantified by the photocount and photon noise-reduction-parameters R_c and R_n depend only weakly on the number N of grouped detection windows, as shown in Fig. 3(c). Whereas the values of the photocount noise-reduction-parameters R_c are around 0.7, in agreement with the detection efficiencies of the APDs used, the values of the noise-reduction-parameters R_n of the compound TWBs reconstructed by the ML approach are close to 0, indicating nearly ideal pairing of the signal and idler photons.

The covariances C_c and C_n of the photocount and photon numbers, respectively, are plotted in Fig. 3(d). Whereas the covariances C_n of the reconstructed compound TWBs are close to the maximum allowed value of 1 (excluding the TWB with $N = 1$, which is not suitable for ML reconstruction), the values of the photocount covariances C_c gradually increase with an increasing number N of grouped detection windows. They are close to 1 for sufficiently large numbers N of grouped detection windows. This behavior follows from a simple model of N independent constituting TWBs, each being described by the signal and idler photocount numbers c_{sj} and c_{ij} , $j = 1, \dots, N$. The overall photocount numbers $c_a = \sum_{j=1}^N c_{aj}$, $a = s, i$, then have moments $\langle c_s c_i \rangle = N(N-1) \langle c_s \rangle^w \langle c_i \rangle^w + N \langle c_s c_i \rangle^w$ and $\langle c_a^2 \rangle = N(N-1) [\langle c_a \rangle^w]^2 + N \langle c_a^2 \rangle^w$, $a = s, i$, expressed in terms of the moments of the individual constituting TWBs $\langle c_a \rangle^w$, $\langle c_a^2 \rangle^w$, $a = s, i$, and $\langle c_s c_i \rangle^w$. Whereas we have $C_c = [\langle c_s c_i \rangle^w] / [\sqrt{\langle c_s^2 \rangle^w \langle c_i^2 \rangle^w}]$ for $N = 1$ constituting TWB, $C_c \rightarrow 1$ in the limit of a large number N of constituting TWBs.

The intensities of the compound TWBs analyzed in Fig. 3 vary by 3 orders of magnitude: the weakest TWB analyzed, formed by just one constituting TWB and detected in one detection window, contains 0.102 mean photon pairs; the strongest compound TWB, composed of 1000 constituting TWBs and thus detected in 1000 detection windows, is composed of 102 photon pairs. Whereas the contribution of the vacuum state prevails in the weakest TWB, the joint photon-number distribution p_{si} of the strongest compound TWB analyzed exhibits a well-developed pairwise structure localized around the mean photon values [compare Figs. 4(a) and 4(b)]. These two

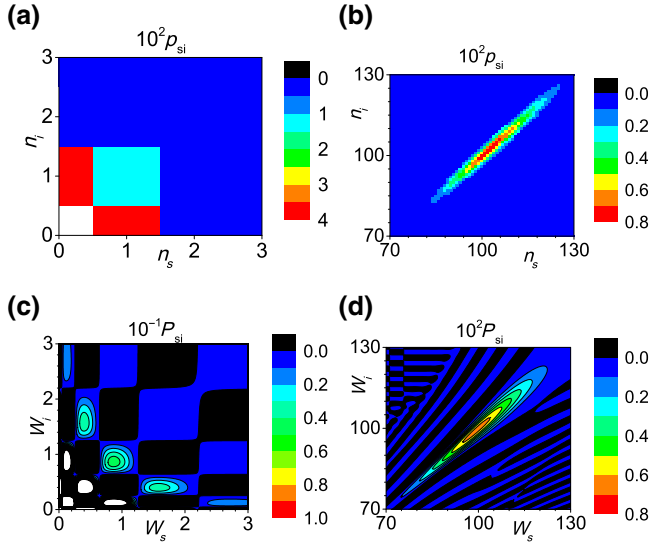


FIG. 4. (a),(b) Photon-number distributions $p_{si}(n_s, n_i)$ and (c),(d) corresponding quasidistributions $P_{si,s}(W_s, W_i)$ of integrated intensities for $N = 1$ [(a), (c)] and $N = 1000$ [(b), (d)]. In (c) [(d)], $s = 0.5$ [$s = 0$]. In (a),(c), the values in the white areas are greater than those explicitly indicated on the z scale.

types of photon-number distribution represent in a certain sense the limiting cases of very weak TWBs (with mean photon-pair numbers much lower than 1) and stronger TWBs with properties developed towards the “classical limit” (with mean photon-pair numbers in the hundreds). Significant differences in their properties, as discussed below, originate from their joint quasidistributions P_{si} of integrated intensities. We recall here that integrated intensities are introduced in the detection theory [3] in which the moments of the integrated intensities refer to the normally ordered photon-number moments. The quasidistributions of the integrated intensities for a given field-operator ordering parameter s are derived from the corresponding quasidistributions of field amplitudes defined in the field phase space. The quasidistributions of the integrated intensities for s -ordered field operators can be determined from the corresponding joint photon-number distributions p_{si} using the formula [3]

$$\begin{aligned}
 & P_{si,s}(W_s, W_i) \\
 &= \frac{4}{(1-s)^2} \exp\left(-\frac{2(W_s + W_i)}{1-s}\right) \sum_{n_s, n_i=0}^{\infty} \frac{p_{si}(n_s, n_i)}{n_s! n_i!} \\
 & \quad \times \left(\frac{s+1}{s-1}\right)^{n_s+n_i} L_{n_s}\left(\frac{4W_s}{1-s^2}\right) L_{n_i}\left(\frac{4W_i}{1-s^2}\right), \quad (17)
 \end{aligned}$$

in which the symbol L_k denotes the k th Laguerre polynomial [38]. In the quasidistribution P_{si} of the weakest TWB, plotted in Fig. 4(c), there occur local positive peaks and

negative dips, forming a structure with typical rays running from the beginning $(W_s, W_i) = (0, 0)$ and parabolas. On the other hand, a ray structure with a global positive maximum around the diagonal and negative “valleys” sandwiched between positive local maxima characterize the quasidistribution P_{si} of the strongest compound TWB analyzed and plotted in Fig. 4(d). This reflects a well-formed pairwise character of the compound TWB with 102 mean photon pairs.

IV. ANALYSIS OF EFFECTIVE DETECTION EFFICIENCY

Before we analyze the statistical properties of compound TWBs and their applications, we have to address first the effective detection efficiencies of the PNRDs used in TWB detection. The effective detection efficiency η_s^{eff} of a PNRD is an important parameter when experimental TWBs are analyzed. It arises from a generalization [20,39] of the Klyshko method [18] for the determination of the absolute detection efficiency developed originally for individual photon pairs. In fact, it gives a refined effective value for the usual overall detection efficiency that involves, in a real experiment, the absolute quantum detection efficiency of the detector (estimated at 0.80 for the APDs used and the appropriate wavelength) and the losses on the way from the field source to the detector (dominantly caused by fiber coupling, with an estimated coupling efficiency below 0.35). This generalization suggests an appropriate effective detection efficiency η_s^{eff} of the signal detector in the form

$$\eta_s^{\text{eff}} = \frac{\langle \Delta c_s \Delta c_i \rangle}{\langle c_i \rangle}. \quad (18)$$

The effective detection efficiency η_s^{eff} depends on the properties of the TWB and is affected by, among other things, the pump-pulse intensity fluctuations and the TWB noise.

We first reveal the limitation of the formula in Eq. (18) by considering an intense genuine TWB described by the photon-number distribution p_{si} in Eq. (4). Assuming detection of such a TWB by detectors with detection efficiencies η_s and η_i and using the Mandel detection formula, the correlation function $\langle \Delta c_s \Delta c_i \rangle = \eta_s \eta_i (\langle \mathcal{W}_p \rangle + \langle (\Delta \mathcal{W}_p)^2 \rangle)$ [$\langle \mathcal{W}_a \rangle = M_a B_a$ for $a = p, s, i$, $\langle (\Delta \mathcal{W}_p)^2 \rangle = M_p B_p^2$], depends only on the paired component of the genuine TWB described by the integrated intensity \mathcal{W}_p [39]. On the other hand, the mean idler photocount number $\langle c_i \rangle = \eta_i [\langle \mathcal{W}_p \rangle + \langle \mathcal{W}_i \rangle]$ also depends on the noise idler component, with an integrated intensity \mathcal{W}_i . Under these conditions, the effective detection efficiency η_s^{eff} in Eq. (18) is derived in the form

$$\eta_s^{\text{eff}} = \eta_s \frac{\langle \mathcal{W}_p \rangle + \langle (\Delta \mathcal{W}_p)^2 \rangle}{\langle \mathcal{W}_p \rangle + \langle \mathcal{W}_i \rangle}. \quad (19)$$

According to Eq. (19), if a TWB is noiseless [$\langle \mathcal{W}_i \rangle = 0$] is the photon-pair statistics are Poissonian [$\langle (\Delta \mathcal{W}_p)^2 \rangle = 0$] [3], we have $\eta_s^{\text{eff}} = \eta_s$ directly. Otherwise, photon-pair-number fluctuations exceeding the Poissonian ones increase the effective efficiency η_s^{eff} . Noise acts in the opposite way.

In the experiment, the effective signal- and idler-field detection efficiencies η_s^{eff} and η_i^{eff} are more or less constant for numbers N of grouped detection windows up to 100, and then they gradually increase with increasing number N [see Fig. 5(a)]. It follows from the curves in Fig. 5(a) that subtraction of the known dark count rates $D_s = 2.8 \times 10^{-3}$ and $D_i = 3.8 \times 10^{-3}$ from the experimental mean photocount numbers $\langle c_a \rangle$ in Eq. (18) increases the effective detection efficiencies η_a^{eff} , $a = s, i$, by about 2%. On the

other hand, the values of the detection efficiencies $\eta_s = 0.282$ and $\eta_i = 0.330$ used in the theoretical fit to the experimental data in Fig. 5(a) are about 1% greater than the measured effective detection efficiencies η^{eff} for $N \leq 100$. This is a consequence of the small amount of noise present in the experimental compound TWBs. According to the formula in Eq. (19), the theoretical effective detection efficiencies η^{eff} are independent of the number N of grouped detection windows, as both expressions in the numerator and denominator are linearly proportional to the number N of grouped detection windows, as documented by the curves in Fig. 5(a). The effective detection efficiencies η^{eff} appropriate to N -pixel PNRDs behave very similarly, as follows from the curves in Fig. 5(a). This behavior originates from the fact that the mean number of photons impinging on one detection pixel is considerably smaller than 1. However, we note here that for small numbers m_p of paired modes in a constituting TWB (in one detection window), i.e., when the TWB photon-number distribution is close to a thermal one, the efficiencies η^{eff} decrease slightly for small numbers N . This effect is described by the term $\langle (\Delta \mathcal{W}_p)^2 \rangle$ in Eq. (19).

The increase in the effective detection efficiencies η^{eff} for $N \geq 100$ is attributed to correlations in the intra-pump-pulse intensity fluctuations already observed in the graphs of the marginal Fano factors $F_{c,i}$ and $F_{n,i}$ in Fig. 3(b). To quantify these correlations, we determine the normalized correlation function $K_{a,\Delta j}$ of the photocount fluctuations $\Delta c_{a,j}$ and $\Delta c_{a,j+\Delta j}$ of the field a , $a = s, i$, mutually shifted by Δj detection windows for a large number N_M of measurement repetitions:

$$K_{\Delta j} = N_M \frac{\sum_{j=1}^{N_M} \Delta c_{a,j} \Delta c_{a,j+\Delta j}}{[\sum_{j=1}^{N_M} c_{a,j}]^2}. \quad (20)$$

When we process the experimental data, the sum over the index j runs over all detection windows. Random fluctuations of the normalized correlation functions K_s and K_i for $\Delta j \in \langle 980, 1000 \rangle$ are documented in Fig. 5(b). Despite the large relative distance Δj between the detection windows, they tend to exhibit positive correlations. The normalized correlation functions \bar{K}_s and \bar{K}_i averaged over 49 neighboring indices Δj , plotted in Fig. 5(c), clearly express positive correlations for Δj comparable to or greater than 100. On the other hand, negative correlations are observed for Δj smaller than 100. These originate from an electronic response of the detector, in general known as the dead-time effect. The correlations quantified in the graphs in Figs. 5(b) and 5(c) provide suitable values for the parameters of the model for correlations in the intra-pump-pulse intensity fluctuations and compound-TWB generation developed in the Appendix. The resultant curves for the effective detection efficiencies η^{eff} are shown in Fig. 5(a) by plain solid black curves.

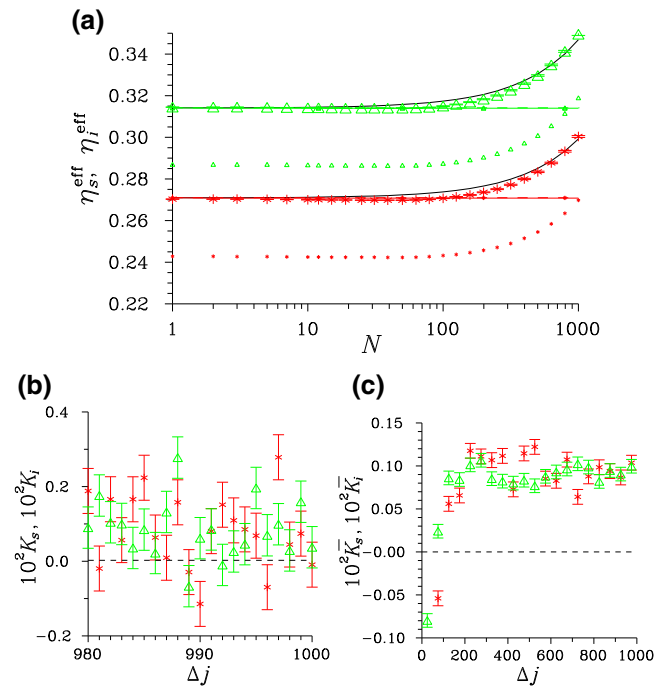


FIG. 5. (a) Effective detection efficiencies η^{eff} obtained with (large symbols) and without (small symbols) subtraction of the detector dark counts, plotted as functions of the number N of grouped detection windows. (b) Normalized photocount correlation functions K and (c) averaged normalized photocount correlation functions \bar{K} depending on the relative distance Δj of the detection windows; $\bar{K}_{\Delta j} \equiv \sum_{\Delta k \in \langle \Delta j - \delta j, \Delta j + \delta j \rangle} K_{\Delta k} / (2\delta j + 1)$. The experimental data are plotted as isolated symbols with error bars [in (a) they are smaller than the plotted symbols] for the signal (red asterisks) and idler (green triangles) detectors. The solid (dashed) curves with symbols in (a) originate from the model of compound (genuine) TWBs detected by APDs (N -pixel PNRDs); the curves nearly coincide. The black plain solid curves in (a) are drawn for the model of compound TWBs with correlations in intra-pump-pulse intensity fluctuations. The dashed horizontal lines in (b),(c) indicate neutral correlations $K = \bar{K} = 0$; $\delta j = 24$.

V. NONCLASSICALITY OF COMPOUND TWIN BEAMS

The most striking property of TWBs is their nonclassicality, which originates from tight correlations between the signal and idler photon numbers [8,40–43]. As the marginal signal and idler beams are classical, the nonclassicality of TWBs in fact reflects the entanglement (quantum correlations) between the signal and idler beams. We note that this entanglement is different from that usually discussed for individual photon pairs in quantum superposition states [2]. For compound TWBs, the amount of overall noise increases linearly with the number of constituting TWBs included, and so the question is to what extent the nonclassicality is preserved for stronger compound TWBs. We show that the nonclassicality of compound TWBs even increases with their intensity, owing to their increasing photon-pair number.

The nonclassicality of TWBs is identified by use of nonclassicality identifiers (NCIs), usually based on nonclassicality inequalities either written in terms of (integrated) intensity moments [44] or containing the probabilities of photon-number (or photocount) distributions [45]. Here, we restrict our attention to NCIs based on intensity moments. The intensity moments $\langle W_s^k W_i^l \rangle$ are derived from the photon-number moments $\langle n_s^m n_i^j \rangle$ using the following formula:

$$\langle W_s^k W_i^l \rangle = \sum_{m=0}^k S(k, m) \sum_{j=0}^l S(l, j) \langle n_s^m n_i^j \rangle, \quad (21)$$

which includes the Stirling numbers S of the first kind [46]. We note that the relations in Eq. (21) between the normally ordered photon-number moments (referred to as intensity moments) and the usual photon-number moments originate from the canonical commutation relations. We also address the nonclassicality of the directly detected photocount distributions f_{si}^c . To do this, we pretend that the photocount distributions f_{si}^c analyzed were obtained with ideal detectors and determine the associated intensity moments $\langle W_s^k W_i^l \rangle_c$ from the photocount moments $\langle c_s^m c_i^j \rangle$ using the formula in Eq. (21).

The intensity NCIs for TWBs were comprehensively analyzed in Ref. [44]. Our motivation here is twofold: first, to study the higher-order nonclassicality indicated by higher-order intensity moments for compound TWBs with intensities varying over 3 orders of magnitude; and second, to identify the best-performing NCIs, especially for greater numbers N of grouped detection windows. In our analysis, the following NCIs containing the intensity moments up to the fifth order were found to be the best [44]:

$$E_{001} \equiv \langle W_s^2 \rangle + \langle W_i^2 \rangle - 2\langle W_s W_i \rangle < 0, \quad (22)$$

$$E_{101} \equiv \langle W_s^3 \rangle + \langle W_s W_i^2 \rangle - 2\langle W_s^2 W_i \rangle < 0, \quad (23)$$

$$E_{111} \equiv \langle W_s^3 W_i \rangle + \langle W_s W_i^3 \rangle - 2\langle W_s^2 W_i^2 \rangle < 0, \quad (24)$$

$$E_{211} \equiv \langle W_s^4 W_i \rangle + \langle W_s^2 W_i^3 \rangle - 2\langle W_s^3 W_i^2 \rangle < 0. \quad (25)$$

Only the following two NCIs derived from the matrix approach were capable of indicating the nonclassicality of the directly measured photocount distributions f_{si}^c for greater numbers N of grouped detection windows:

$$M_{1001} \equiv \langle W_s^2 \rangle \langle W_i^2 \rangle - \langle W_s W_i \rangle^2 < 0, \quad (26)$$

$$M_{001001} \equiv \langle W_s^2 \rangle \langle W_i^2 \rangle + 2\langle W_s W_i \rangle \langle W_s \rangle \langle W_i \rangle - \langle W_s W_i \rangle^2 - \langle W_s^2 \rangle \langle W_i \rangle^2 - \langle W_s \rangle^2 \langle W_i^2 \rangle < 0. \quad (27)$$

The above NCIs can even be used for quantifying the nonclassicality when the corresponding Lee nonclassicality depths (NCDs) [47] are determined. To do this, we first determine the intensity moments $\langle W_s^k W_i^l \rangle_s$ related to a general s -ordering of the field operators from the normally ordered intensity moments $\langle W_s^k W_i^l \rangle$ using the coefficients of the Laguerre polynomials L_k [3]:

$$\langle W_s^k W_i^l \rangle_s = \left(\frac{1-s}{2} \right)^{k+l} \left\langle L_k \left(\frac{2W_s}{s-1} \right) L_l \left(\frac{2W_i}{s-1} \right) \right\rangle. \quad (28)$$

Then we apply the above NCIs, written directly for the s -ordered intensity moments $\langle W_s^k W_i^l \rangle_s$. The nonclassicality indicated by the NCIs is gradually suppressed with decreasing values of the ordering parameter s due to the increasing detection noise related to the operator ordering. Using this, we look for the threshold value s_{th} at which a given NCI is nullified. This gives the border between quantum and classical behavior. The corresponding NCD τ is derived as follows [47]:

$$\tau = \frac{1 - s_{\text{th}}}{2}. \quad (29)$$

This gives the smallest mean number of thermal photons in a noisy field that, when superimposed on the field analyzed, guarantees the suppression of nonclassicality of the field analyzed. It holds that $0 < \tau \leq 1/2$ for any nonclassical two-dimensional Gaussian field.

Whereas the NCIs E defined in Eqs. (22)–(25) identify the nonclassicality for any reconstructed compound TWB, they fail to resolve the nonclassicality directly contained in the corresponding photocount distributions f_{si}^c belonging to stronger compound TWBs (for $N \geq 800$), as documented by the curves of the NCDs $\tau_{E,c}$ and $\tau_{E,n}$ in Figs. 6(a) and 6(b). This is a consequence of the noise present in the TWB photocount distributions f_{si}^c , whose level increases linearly with the number N of grouped detection windows. The values of the NCDs $\tau_{E,c}$ and $\tau_{E,n}$ reached decrease slightly with increasing order of the intensity moments involved. Nevertheless, the NCDs $\tau_{E,n}$ for the reconstructed compound TWBs tend to approach

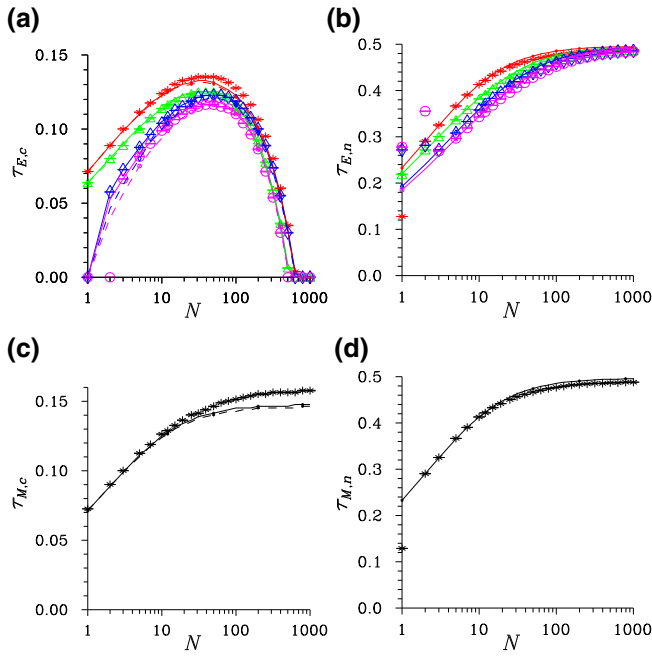


FIG. 6. Nonclassicality depths for (a,c) the joint photocount (τ_c) and (b,d) the joint photon-number (τ_n) distributions depending on the number N of grouped detection windows. The NCIs E_{001} (red asterisks), E_{101} (green triangles), E_{111} (blue diamonds), and E_{211} (magenta circles) are used in (a,b); the NCI M_{1001} (asterisks) is shown in (c,d). The experimental data are plotted by isolated symbols; their error bars are smaller than the plotted symbols. The solid (dashed) curves originate from the model of compound (genuine) TWBs detected by APDs (N -pixel PNRDs); the solid and dashed curves nearly coincide.

values close to the maximum allowed value of $1/2$ for large numbers N of grouped detection windows. On the other hand, maximum values of the NCDs $\tau_{E,c}$ for the photocount distributions f_{si}^c close to 0.14 are reached for N around 50 .

The NCIs M given in Eqs. (26) and (27) reveal the nonclassicality also for the photocount distributions f_{si}^c of strong compound TWBs, as shown in Fig. 6(c) for the NCI M_{1001} . Moreover, the values of the NCDs $\tau_{M,c}$ obtained increase with the number N of grouped detection windows, similarly to those of the NCDs $\tau_{M,n}$ appropriate for the reconstructed compound TWBs [Fig. 6(d)]. We note that the values of the NCDs τ_M belonging to the NCIs in Eqs. (26) and (27) are, for the compound TWBs analyzed, very close to each other independently of the number N . As the NCI M_{001001} in Eq. (27) has a more complex structure than the NCI M_{1001} in Eq. (26), it is more prone to experimental errors. That is why we prefer to use the NCI M_{1001} for identification of the nonclassicality of compound TWBs of arbitrary intensity. Both of the theoretical models for TWBs and their detection give good predictions for the NCDs τ derived from the photon-number and photocount distributions, as shown in Fig. 6: the model of compound

TWBs detected by APDs predicts slightly larger values of the NCDs τ for the photocount distributions compared with the model of genuine TWBs detected by N -pixel PNRDs (a stronger pileup effect).

VI. GENERATION OF SUB-POISSONIAN LIGHT

Compound TWBs may also be used for efficient generation of sub-Poissonian light via postselection. Postselection with PNRDs applied to TWBs is, together with cavity-quantum-electrodynamics schemes [48], one of the most efficient methods of generation of sub-Poissonian light with greater photon numbers, in both the cw [27,28,49] and the pulsed [11,29,41,50,51] regime. However, for realistic PNRDs, the method gradually loses its potential with increasing postselection photocount number, which limits the maximum intensities of the generated sub-Poissonian fields. Here, we address this limitation for compound TWBs and APDs.

An idler field conditioned by the detection of c_s signal photocounts is experimentally characterized by the conditional photocount histogram $f_{c,i}^c(c_i; c_s)$ derived from the joint signal-idler photocount histogram $f_{si}^c(c_s, c_i)$ by appropriate normalization:

$$f_{c,i}^c(c_i; c_s) = \frac{f_{si}^c(c_s, c_i)}{\sum_{c'_i=0}^{\infty} f_{si}^c(c_s, c'_i)}. \quad (30)$$

The corresponding conditional idler photon-number distributions $p_{c,i}^c(n_i; c_s)$ can then be obtained using the ML approach, similarly to the case of TWBs. The looked-for distribution $p_{c,i}^c(n_i; c_s, N)$ obtained from a compound TWB formed by N constituting TWBs (detected in N detection windows of APDs) is found as a steady state of the following iteration procedure (where j stands for the iteration index):

$$p_{c,i}^{c(j+1)}(n_i; c_s, N) = \sum_{c_i=0}^{\infty} F_i^{(j)}(c_i; c_s, N) T_i(c_i, n_i; N),$$

$$F_i^{(j)}(c_i; c_s, N) = f_{c,i}^c(c_i; c_s, N) \left[\sum_{n'_i=0}^{\infty} T_i(c_i, n'_i; N) \times p_{c,i}^{c(j)}(n'_i; c_s, N) \right]^{-1}, \quad j = 0, 1, \dots \quad (31)$$

The sub-Poissonianity is quantified by the Fano factor F defined in Eq. (14), which naturally depends on the conditioning signal photocount number c_s . Detailed inspection [14,29] reveals the following behavior, which reflects the limited detection efficiency and the presence of

dark counts in the postselecting detector: with an increasing conditioning signal photocount number c_s , the values of the Fano factor F first decrease naturally, they reach a minimum, and then they increase at greater signal photocount numbers c_s that have a very low probability of detection. As we are interested in the potential of the postselection scheme to generate the most nonclassical states possible, we analyze further the values of the Fano factor at this minimum.

With an increasing number N of grouped detection windows, the intensity of the compound TWBs increases, the optimal conditioning signal photocount number c_s increases [Fig. 7(c)], and, as a consequence, the mean idler photocount ($\langle c_{c,i} \rangle$) and photon ($\langle n_{c,i} \rangle$) numbers of the postselected fields monotonically increase, as quantified in Fig. 7(a). Unfortunately, the accompanying photocount and photon-number Fano factors $F_{c_{c,i}}$ and $F_{n_{c,i}}$, respectively, also increase with the increasing number N of grouped detection windows [see Fig. 7(b)]. This increase originates from the increasing level of overall noise in the postselecting signal detector with an increasing number N of grouped detection windows. This noise has a strong detrimental influence on the performance of the postselection scheme. Whereas the idler field postselected by detecting in just one detection window has around 1 photon and a Fano factor around 0.2, the idler field postselected by detection in 1000 grouped detection windows contains around 100 photons, but its Fano factor is only around 0.7. We note that the teeth in the curves of the Fano factors F in Fig. 7(b) are caused by the discrete values of the optimal conditioning signal photocount numbers c_s . The scheme for the generation of sub-Poissonian light analyzed here is probabilistic, and the probability p_{c_s} of success decreases in general with the number N of grouped detection windows. However, as follows from the curve in Fig. 7(d), the probability p_{c_s} of success is in the range of a few percent even for the strongest compound TWBs analyzed.

Similarly to the case of compound TWBs, we address the nonclassicality of the conditional idler fields $p_{c,i}^c$ using NCIs based on intensity moments up to the fifth order. Relying on the results of Ref. [52], we apply the following fundamental NCIs:

$$L_{k1}^1 = \langle W^{k+1} \rangle - \langle W^k \rangle \langle W \rangle < 0, \quad k = 1, \dots, 4. \quad (32)$$

We note that the commonly used NCIs $\langle W^k \rangle - \langle W \rangle^k < 0$, $k = 2, \dots, 5$, are derived with the help of the NCIs in Eq. (32). We can see in Figs. 7(e) and 7(f) that the photocount NCDs $\tau_{L,c,i}$ and the photon NCDs $\tau_{L,n,i}$ gradually decrease with an increasing number N of grouped detection windows, i.e., with increasing intensity of the postselected idler fields. Whereas the values of the NCDs $\tau_{L,i}$ attained drop considerably with the order of the intensity moments involved in the NCIs for smaller numbers N , the values of the NCDs $\tau_{L,i}$ are close to each other for

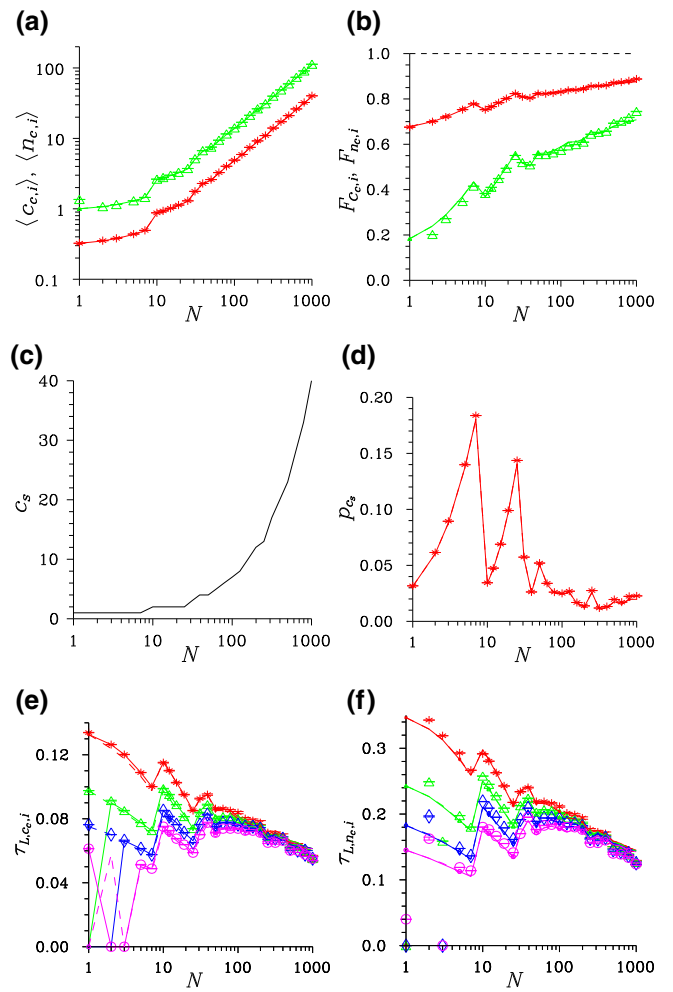


FIG. 7. (a) Mean number of idler photons $\langle n_{c,i} \rangle$ (photocounts $\langle c_{c,i} \rangle$), (b) Fano factor $F_{n_{c,i}}$ ($F_{c_{c,i}}$), (c) optimal conditioning signal photocount number c_s , and (d) its probability p_{c_s} of detection. (e) [(f)] photocount- [photon]-number NCDs $\tau_{L,c,i}$ [$\tau_{L,n,i}$] for NCIs L_{11}^1 (red asterisks), L_{21}^1 (green triangles), L_{31}^1 (blue diamonds), and L_{41}^1 (magenta circles) belonging to conditional idler fields $p_{c,i}^c$ generated after registering the c_s optimal signal photocounts indicated in (c), depending on the number N of grouped detection windows. In (a),(b),(d), isolated symbols with error bars (smaller than the plotted symbols) are drawn for the experimental photocount histograms (red asterisks) and the fields reconstructed by the ML approach (green triangles). The experimental data plotted in (e),(f) by isolated symbols have error bars smaller than the symbols used. The solid (dashed) curves arise from the model of compound (genuine) TWBs detected by APDs (N -pixel PNRDs). In (a),(b),(d),(e),(f), the solid and dashed curves nearly coincide. The horizontal plain dashed line in (b) indicates the nonclassicality border $F = 1$.

greater numbers N . In Figs. 7(e) and 7(f), the values of the photon NCDs $\tau_{L,n,i}$ reached are about 3 times greater than the values of the corresponding photocount NCDs $\tau_{L,c,i}$, in agreement with the detection efficiency $\eta_i = 0.33$.

We note that the models of compound TWBs detected by APDs [see Eq. (11)] and genuine TWBs detected by N -pixel PNRDs give, apart from the case of small numbers N , very similar predictions of the quantities characterizing the postselected sub-Poissonian fields that are in good agreement with the experimental results, as documented in the graphs in Fig. 7.

VII. SUB-SHOT-NOISE MEASUREMENT OF ABSORPTION

As we have seen in the previous section, postselection with compound TWBs gives compound sub-Poissonian fields with reduced photon-number fluctuations. When applied to the measurement of absorption coefficients [23, 24, 30, 33, 34], they provide sub-shot-noise precision, i.e., precision better than the classical optimal limit reached by coherent states with their Poissonian photon-number statistics. Below, we show that the measurement precision increases with increasing intensity of a compound TWB.

The determination of the mean values $\langle c \rangle$ of photocounts is the essence of the measurement of absorption coefficients. The mean photocount numbers $\langle c \rangle$ are measured for the fields in front of and beyond the sample, and their ratio gives the looked-for absorption coefficient. The precision (uncertainty) of such a measurement is quantified by the relative error δc given by

$$\delta c = \frac{\sqrt{\langle (\Delta c)^2 \rangle_m}}{\langle c \rangle_m}, \quad (33)$$

where the symbol $\langle \rangle_m$ denotes averaging over the finite experimental data set obtained. If a coherent state with mean photocount number $\langle c \rangle_{cl}$ and Poissonian photocount statistics [$\langle (\Delta c)^2 \rangle_{cl} = \langle c \rangle_{cl}$] is applied N_M times, the corresponding relative error δc_{cl} takes the form

$$\delta c_{cl} = \frac{1}{\sqrt{\langle c \rangle_{cl} N_M}}. \quad (34)$$

This serves as a reference in the definition of the normalized relative error $\delta_{r,c}$:

$$\delta_{r,c} = \frac{\delta c}{\delta c_{cl}}. \quad (35)$$

Sub-shot-noise measurements are characterized by $\delta_{r,c} < 1$.

To demonstrate the ability of compound TWBs to overcome the classical limit of Eq. (34), we analyze two data sets in parallel. Speaking about the idler detector, we consider a sequence of idler detections in all detection windows as a reference. The second sequence contains idler detections only in the detection windows in which a signal photocount is registered. If we sum the photocount numbers c_i in N successive detection windows in the first

reference sequence, we arrive at a photocount histogram characterizing the marginal idler field of a compound TWB formed by N constituting TWBs. On the other hand, summation of the conditioned photocount numbers $c_{c,i}$ over N successive detection windows in the second sequence provides us with a photocount histogram of the idler field conditioned by the detection of N signal photocounts in N grouped detection windows (forming a compound TWB). This field is sub-Poissonian and overcomes the classical limit of Eq. (34).

To experimentally quantify the dependence of the measurement precision on the number N_M of measurement repetitions, we determine the following experimental relative error:

$$\delta c(N_M) = \left\langle \sqrt{\frac{\sum_{j=1}^{N_M} c_j^2 / N_M - \left(\sum_{j=1}^{N_M} c_j / N_M \right)^2}{\sum_{j=1}^{N_M} c_j / N_M}} \right\rangle_m. \quad (36)$$

However, we have to consider sufficiently large numbers N_M of measurement repetitions to arrive at reliable (acceptable) values of the relative errors δc . We illustrate this behavior in Fig. 8, where the normalized relative error δ_{r,c_i} of the idler photocount numbers c_i summed over $N = 200$ detection windows is plotted. The values of the normalized relative error δ_{r,c_i} for numbers N_M of measurement repetitions smaller than 10 are, although with large absolute experimental errors, artificially smaller than the correct value found for asymptotically large numbers N_M . The data shown in Fig. 8 suggest that numbers N_M of measurement repetitions greater than 100 provide reliable values of the mean photocount number $\langle c_i \rangle$ for the idler field analyzed ($\langle c_i \rangle = 7.463 \pm 0.002$).

According to Eq. (34), the relative error δc decreases with increasing field intensity, i.e., with increasing mean photocount number $\langle c \rangle$. Working with the compound TWBs, the mean photocount numbers $\langle c \rangle$ increase linearly with the number N of grouped detection windows. These

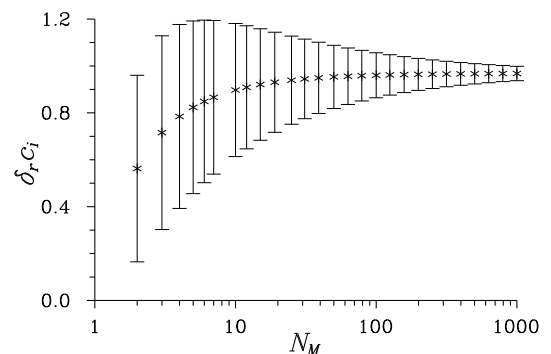


FIG. 8. Normalized relative error δ_{r,c_i} of the idler photocount number for $N = 200$ grouped detection windows depending on the number N_M of measurement repetitions. The relative experimental errors of δ_{r,c_i} plotted are given by $1/\sqrt{N_M}$.

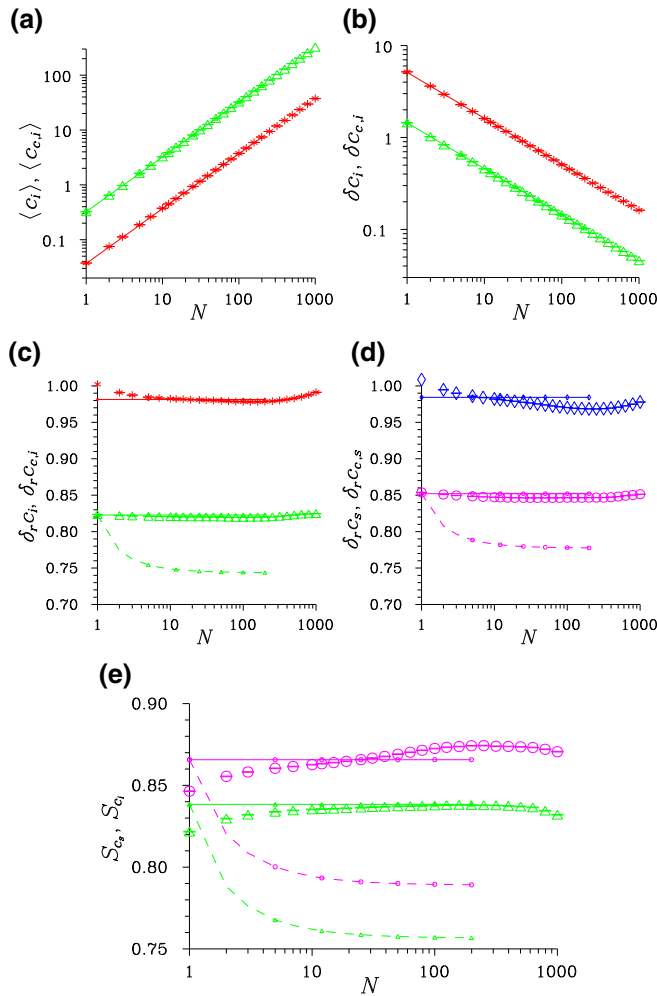


FIG. 9. (a) Mean numbers of idler photocounts $\langle c_i \rangle$ and conditioned idler photocounts $\langle c_{c,i} \rangle$; (b) the corresponding relative errors δc_i and $\delta c_{c,i}$; (c) [(d)] normalized relative errors $\delta_r c_i$ [$\delta_r c_s$] and $\delta_r c_{c,i}$ [$\delta_r c_{c,s}$]; and (e) ratios S_{c_s} and S_{c_i} of normalized relative errors, depending on the number N of grouped detection windows. The isolated symbols with error bars (smaller than the plotted symbols) originate from the experiment with signal [idler] photocounts (blue diamonds [red asterisks]) and signal [idler] conditioned photocounts (magenta circles [green triangles]). The solid (dashed) curves are given by the model of compound (genuine) TWBs detected by APDs (N -pixel PNRDs); $N_M = 500$.

dependencies are shown in Figs. 9(a) and 9(b) for the idler photocount numbers c_i (from the reference sequence) and the conditioned idler photocount numbers $c_{c,i}$. For a given number N of grouped detection windows, the mean conditioned photocount numbers $c_{c,i}$ are about 10 times greater than the mean photocount numbers c_i of the reference sequence [see Fig. 9(a)], which is given by the parameters of the postselection scheme. On the other hand, the relative errors $\delta c_{c,i}$ of the conditioned photocounts are more than $\sqrt{10}$ times smaller than the relative errors δc_i of the photocounts from the reference sequence [see Fig. 9(b)].

The reduction of the relative error $\delta c_{c,i}$ of the conditioned photocounts with respect to the relative error δc_i of the reference sequence by more than $\sqrt{\langle c_{c,i} \rangle / \langle c_i \rangle}$ is caused by the sub-Poissonian character of the conditioned idler photocount fields. To separate out the effect of the field intensity on the relative errors, we plot in Figs. 9(c) and 9(d) the normalized relative errors $\delta_r c_i$ and $\delta_r c_{c,i}$ for the idler fields together with their signal counterparts $\delta_r c_s$ and $\delta_r c_{c,s}$. The values of the normalized relative errors $\delta_r c_s$ and $\delta_r c_i$ for the photocounts of the reference sequence at the signal and idler detectors, respectively, are slightly below 1. The multimode thermal character of the detected marginal signal and idler fields in the reference sequence suggests that the values of these normalized relative errors should be slightly above 1, but the effect of pileup in the detection in individual detection windows leads to values slightly smaller than 1. On the other hand, the normalized relative errors $\delta_r c_{c,s} \approx 0.82$ and $\delta_r c_{c,i} \approx 0.85$ of the conditioned photocounts express increased measurement precision due to the sub-Poissonian character of the conditioned photocount fields.

To quantify the improvement in the measurement precision due to the application of such compound sub-Poissonian fields, we show in Fig. 9(e) the ratios S_{c_s} and S_{c_i} of the conditioned photocount normalized relative errors and their counterparts in the reference signal and idler sequences:

$$S_{c_a} = \frac{\delta_r c_{c,a}}{\delta_r c_a}, \quad a = s, i. \quad (37)$$

In our experiment and according to the curves in Fig. 9(e), the improvement in the measurement precision of the absorption coefficient lies in the range from 12% to 17%. A better improvement is observed at the idler detector, as the idler detection efficiency η_i is greater than the signal detection efficiency η_s . The ratios S_{c_s} and S_{c_i} increase slightly with the number N of grouped detection windows. This is caused by the increasing level of noise with an increasing number N of grouped detection windows caused by the correlations in the intra-pump-pulse intensity fluctuations already discussed in relation to the Fano factors of the marginal fields and effective detection efficiencies. We note that the slight decrease in the values of the ratios S_{c_s} and S_{c_i} close to $N = 1000$ in Fig. 9(e) is caused by the fact that we average over $N_M = 500$ measurement repetitions for technical reasons ($N_M < N$).

In the graphs in Fig. 9, we also plot the curves arising for the models of compound TWBs detected by APDs (solid curves) and genuine TWBs detected by N -pixel PNRDs (dashed curves). The quantities for the photocount fields in the reference sequence are directly derived from the signal and idler marginal fields of compound TWBs formed by N constituting TWBs. On the other hand, the quantities for the conditioned photocount fields originate

from a model of sub-Poissonian fields obtained from compound TWBs formed by N constituting TWBs that are postselected by registering N photocounts in the complementary field. According to the curves in Figs. 9(c)–9(e), the use of genuine TWBs with N -pixel PNRDs instead of the compound TWBs analyzed and detected in N APDs detection windows improves the measurement precision by about 50% for $N > 10$ (signal detector, 13% \rightarrow 21%; idler detector, 16% \rightarrow 25%). This partial degradation in the measurement precision is caused by the structure of the compound TWBs, which, however, allows their simple detection by APDs.

We note that we use the shot-noise limits of the detectors applied, with limited detection efficiencies, as a reference and beat this limit by the use of generated compound sub-Poissonian fields. If detectors with detection efficiencies close to 1 are used, the experimental scheme analyzed would allow one to beat the ultimate shot-noise limit set for an ideal detector. This has been reached, e.g., in Ref. [24].

VIII. CONCLUSIONS

We suggest a scheme for substituting genuine multi-mode twin beams by compound twin beams. The compound twin beams are composed of constituting twin beams that replace the fields in individual spatio-spectral modes of the genuine twin beams. The constituting twin beams are sufficiently weak so that they allow detection by single-photon-sensitive *on-off* detectors. As a consequence, the photocount statistics of the compound twin beams are revealed without the need of photon-number-resolving detectors.

We experimentally analyze the properties of compound twin beams containing up to hundreds of photon pairs, side by side with appropriate theoretical models. The marginal Fano factors, noise-reduction parameters, and covariances of photon numbers determined reveal a close similarity with genuine twin beams. We determine the effective detection efficiencies for the compound twin beams.

Using experimental compound twin beams with intensities varying over 3 orders of magnitude, we identify nonclassicality identifiers suitable for stronger twin beams and, by determining the corresponding nonclassicality depths, we confirm the highly nonclassical properties of stronger compound twin beams.

Using compound twin beams and postselection based on measurement of the photocounts in one beam, we experimentally generate sub-Poissonian fields with intensities of up to 100 photons and systematically study their properties, including quantification of the nonclassicality. However, we experimentally demonstrate that the real postselection scheme loses efficiency with increasing field intensity.

We experimentally demonstrate the ability to use compound twin beams to perform sub-shot-noise measurements of absorption. Though compound twin beams are less convenient than genuine twin beams in this measurement, the use of single-photon sensitive *on-off* detectors in their detection represents a huge advantage, from the point of view of both their operation and high absolute detection efficiencies. Sub-shot-noise imaging with compound twin beams is especially promising for the imaging of biological and other samples prone to the effects of light illumination. The broad spectra of twin beams also allow spectroscopy measurements with sub-shot-noise precision.

ACKNOWLEDGMENTS

The authors thank the GA ĀR Project No. 18-22102S. They also acknowledge support from MŠMT ĀR (Project No. CZ.1.05/2.1.00/19.0377).

APPENDIX: MODEL FOR CORRELATED INTRA-PUMP-PULSE INTENSITY FLUCTUATIONS AND COMPOUND-TWIN-BEAM GENERATION

A comparison of the measured effective detection efficiencies η^{eff} and the marginal photocount Fano factors F_c , shown in Figs. 5(a) and 3(b), respectively, with their theoretical counterparts shows that there occurs some additional noise that affects compound TWBs detected in more than 100 detection windows. This additional noise is linearly proportional to the number N of detection windows for $N \geq 100$. As it affects the measured effective detection efficiencies η^{eff} , it has to be of “paired” origin. We attribute this noise to correlations of the pump-pulse intensity fluctuations among successive pulses. These pump-pulse intensity fluctuations are transferred in the process of spontaneous parametric down-conversion into fluctuations of the integrated intensity of the paired component of a TWB (the photon-pair number). This then primarily affects quantities directly depending on the strength of the correlations of the signal and idler fields (the detection efficiencies η^{eff}) and, secondarily, quantities depending solely on the signal or the idler field via the accompanying marginal noise.

To account for such correlations in the pump-pulse intensity fluctuations in the first model of compound TWBs detected by APDs, we consider the following classical statistical Gaussian model for the additional correlated intensity fluctuations $w_{p,j}$ and $w_{p,k}$ of the TWB paired components in detection windows j and k :

$$\begin{aligned} \langle w_{p,j} \rangle_w &= 0, \\ \langle w_{p,j} w_{p,k} \rangle_w &= (1 - \delta_{jk}) K \langle \mathcal{W}_p^w \rangle^2. \end{aligned} \quad (\text{A1})$$

In writing Eq. (A1), we assume that the strength of the additional intensity fluctuations $w_{p,j}$ is linearly proportional to the mean intensity $\langle \mathcal{W}_p^w \rangle$ of the TWB paired component belonging to one detection window. Provided that the detector dark-count rates can be neglected, the value of the phenomenological constant K introduced in the second relation in Eq. (A1) can be estimated from the averaged values of the coefficients \bar{K}_s and \bar{K}_i shown in Fig. 5(c).

The integrated intensity $\mathcal{W}_p^{\text{all}}$ of the paired component of a compound TWB originating from N grouped detection windows and involving the additional intensity fluctuations is determined as $\mathcal{W}_p^{\text{all}} \equiv \mathcal{W}_p + \sum_{j=1}^N w_{p,j}$. Its moments with respect to the additional pump-pulse intensity fluctuations take the form

$$\begin{aligned} \langle \mathcal{W}_p^{\text{all}} \rangle_w &= \langle \mathcal{W}_p \rangle, \\ \langle [\mathcal{W}_p^{\text{all}}]^2 \rangle_w &= \langle \mathcal{W}_p^2 \rangle + KN(N-1) \langle \mathcal{W}_p^w \rangle^2. \end{aligned} \quad (\text{A2})$$

The original formula in Eq. (19) for the signal effective detection efficiency η_s^{eff} is then modified into the form

$$\eta_s^{\text{eff}} = \eta_s \frac{\langle \mathcal{W}_p \rangle + \langle (\Delta \mathcal{W}_p)^2 \rangle + KN(N-1) \langle \mathcal{W}_p^w \rangle^2}{\langle \mathcal{W}_p \rangle + \langle \mathcal{W}_i \rangle}. \quad (\text{A3})$$

Similarly, the signal photocount Fano factor $F_{c,s}$ defined in Eq. (14) is expressed in this model as follows:

$$\begin{aligned} F_{c,s} &= 1 + \eta_s \left[\langle (\Delta \mathcal{W}_p)^2 \rangle + \langle (\Delta \mathcal{W}_s)^2 \rangle \right. \\ &\quad \left. + KN(N-1) \langle \mathcal{W}_p^w \rangle^2 \right] \left[\langle \mathcal{W}_p \rangle + \langle \mathcal{W}_s \rangle \right]^{-1}. \end{aligned} \quad (\text{A4})$$

Also, the formula in Eq. (15) for the noise-reduction-parameter R_c of the photocounts can be appropriately modified:

$$\begin{aligned} R_c &= 1 + \left[(\eta_s - \eta_i)^2 \left[\langle (\Delta \mathcal{W}_p)^2 \rangle + KN(N-1) \langle \mathcal{W}_p^w \rangle^2 \right] \right. \\ &\quad \left. - 2\eta_s \eta_i \langle \mathcal{W}_p \rangle + \eta_s^2 \langle (\Delta \mathcal{W}_s)^2 \rangle + \eta_i^2 \langle (\Delta \mathcal{W}_i)^2 \rangle \right] \\ &\quad \times \left[(\eta_s + \eta_i) \langle \mathcal{W}_p \rangle + \eta_s \langle \mathcal{W}_s \rangle + \eta_i \langle \mathcal{W}_i \rangle \right]^{-1}. \end{aligned} \quad (\text{A5})$$

We note that the corresponding quantities characterizing the photon-number fields are also given by Eqs. (A4) and (A5), in which we set $\eta_s = \eta_i = 1$.

The Fano factors $F_{c,i}$ and $F_{n,i}$ and the effective detection efficiencies η_s^{eff} and η_i^{eff} , which show greater deviations between the experimental data and the predictions of the original model without correlations in the pump-pulse intensity fluctuations for greater numbers N of grouped detection windows, are plotted in Figs. 3(b) and 5(a), respectively. The solid plain curves close to the experimental points in Figs. 3(b) and 5(a), drawn for the model

with correlations in the intra-pump-pulse intensity fluctuations and $K \langle \mathcal{W}_p^w \rangle^2 = 1 \times 10^{-5}$, describe well the behavior of the quantities studied for large numbers N of grouped detection windows. We have $\langle \mathcal{W}_p^w \rangle = m_p b_p = 0.10185$ in the model and so $K = 0.965 \times 10^{-3}$, in accordance with the values of the coefficients \bar{K}_s and \bar{K}_i plotted in Fig. 5(c). As follows from Eq. (A5), the correlations in the pump-pulse intensity fluctuations influence only weakly the values of the noise-reduction parameters R_c and R_n in our case, in which $\eta_s \approx \eta_i$. We note that, in our opinion, the slightly larger theoretical values of the effective detection efficiencies η_s^{eff} and η_i^{eff} in Fig. 5(a) in the area around $N = 100$ indicate longer-range dead-time effects in the response of the APDs and processing electronics used [53].

-
- [1] R. J. McIntyre, Theory of microplasma instability in silicon, *J. Appl. Phys.* **32**, 983 (1961).
 - [2] L. Mandel and E. Wolf, *Optical Coherence and Quantum Optics* (Cambridge University Press, Cambridge, 1995).
 - [3] J. Peřina, *Quantum Statistics of Linear and Nonlinear Optical Phenomena* (Kluwer, Dordrecht, 1991).
 - [4] H. Paul, P. Törmä, T. Kiss, and I. Jex, Photon Chopping: New Way to Measure the Quantum State of Light, *Phys. Rev. Lett.* **76**, 2464 (1996).
 - [5] D. Achilles, Ch. Silberhorn, C. Sliwa, K. Banaszek, and I. A. Walmsley, Fiber-assisted detection with photon number resolution, *Opt. Lett.* **28**, 2387 (2003).
 - [6] M. J. Fitch, B. C. Jacobs, T. B. Pittman, and J. D. Franson, Photon-number resolution using time-multiplexed single-photon detectors, *Phys. Rev. A* **68**, 043814 (2003).
 - [7] O. Haderka, M. Hamar, and J. Peřina Jr., Experimental multi-photon-resolving detector using a single avalanche photodiode, *Eur. Phys. J. D* **28**, 149 (2004).
 - [8] O. Haderka, J. Peřina Jr., M. Hamar, and J. Peřina, Direct measurement and reconstruction of nonclassical features of twin beams generated in spontaneous parametric down-conversion, *Phys. Rev. A* **71**, 033815 (2005).
 - [9] J. Peřina Jr., M. Hamar, V. Michálek, and O. Haderka, Photon-number distributions of twin beams generated in spontaneous parametric down-conversion and measured by an intensified CCD camera, *Phys. Rev. A* **85**, 023816 (2012).
 - [10] G. Chesi, L. Malinverno, A. Allevi, R. Santoro, M. Caccia, and M. Bondani, Measuring nonclassicality with silicon photomultipliers, *Opt. Lett.* **44**, 1371 (2019).
 - [11] G. Harder, T. J. Bartley, A. E. Lita, S. W. Nam, T. Gerrits, and C. Silberhorn, Single-Mode Parametric-Down-Conversion States with 50 Photons as a Source for Mesoscopic Quantum Optics, *Phys. Rev. Lett.* **116**, 143601 (2016).
 - [12] O. S. Magaña-Loaiza, R. de J. León-Montiel, A. Perez-Leija, A. B. U'Ren, C. You, K. Busch, A. E. Lita, S. W. Nam, R. P. Mirin, and T. Gerrits, Multiphoton quantum-state engineering using conditional measurements, *npj Quantum Inf.* **5**, 80 (2019).
 - [13] A. J. Miller, S. W. Nam, J. M. Martinis, and A. V. Sergienko, Demonstration of a low-noise near-infrared

- photon counter with multiphoton discrimination, *Appl. Phys. Lett.* **83**, 791 (2003).
- [14] J. Peřina Jr., V. Michálek, and O. Haderka, Higher-order sub-Poissonian-like nonclassical fields: Theoretical and experimental comparison, *Phys. Rev. A* **96**, 033852 (2017).
- [15] I. A. Malkin and V. I. Man'ko, *Dynamical Symmetries and Coherent States of Quantum Systems* (Nauka, Moscow, 1979).
- [16] Ch. C. Gerry and E. E. Hach III, Generation of even and odd coherent states in a competitive two-photon process, *Phys. Lett. A* **174**, 185 (1993).
- [17] S. Friberg, C. K. Hong, and L. Mandel, Measurement of Time Delays in the Parametric Production of Photon Pairs, *Phys. Rev. Lett.* **54**, 2011 (1985).
- [18] D. N. Klyshko, Use of two-photon light for absolute calibration of photoelectric detectors, *Kvantovaya Elektron. (Moscow)* **7**, 1932 (1980).
- [19] A. Migdall, Correlated-photon metrology without absolute standards, *Phys. Today* **52**, 41 (1999).
- [20] G. Brida, I. P. Degiovanni, M. Genovese, M. L. Rastello, and I. R. Berchera, Detection of multimode spatial correlation in PDC and application to the absolute calibration of a CCD camera, *Opt. Express* **18**, 20572 (2010).
- [21] J. Peřina Jr., O. Haderka, A. Allevi, and M. Bondani, Absolute calibration of photon-number-resolving detectors with an analog output using twin beams, *Appl. Phys. Lett.* **104**, 041113 (2014).
- [22] G. Brida, M. Genovese, and I. R. Berchera, Experimental realization of sub-shot-noise quantum imaging, *Nat. Phys.* **4**, 227 (2010).
- [23] M. Genovese, Real applications of quantum imaging, *J. Opt.* **18**, 073002 (2016).
- [24] E. Losero, I. Ruo-Berchera, A. Meda, A. Avella, and M. Genovese, Unbiased estimation of an optical loss at the ultimate quantum limit with twin-beams, *Sci. Rep.* **8**, 7431 (2018).
- [25] B. E. A. Saleh and M. C. Teich, Can the Channel Capacity of a Light-Wave Communication System be Increased by the use of Photon-Number-Squeezed Light? *Phys. Rev. Lett.* **58**, 2656 (1987).
- [26] I. Straka, L. Lachman, J. Hloušek, M. Miková, M. Mičuda, M. Ježek, and R. Filip, Quantum non-Gaussian multiphoton light, *npj Quantum Inf.* **4**, 4 (2018).
- [27] J. G. Rarity, P. R. Tapster, and E. Jakeman, Observation of sub-Poissonian light in parametric downconversion, *Opt. Commun.* **62**, 201 (1987).
- [28] J. Laurat, T. Coudreau, N. Treps, A. Maitre, and C. Fabre, Conditional Preparation of a Quantum State in the Continuous Variable Regime: Generation of a sub-Poissonian State from Twin Beams, *Phys. Rev. Lett.* **91**, 213601 (2003).
- [29] J. Peřina Jr., O. Haderka, and V. Michálek, Sub-Poissonian-light generation by postselection from twin beams, *Opt. Express* **21**, 19387 (2013).
- [30] E. Jakeman and J. G. Rarity, The use of pair production processes to reduce quantum noise in transmission measurements, *Opt. Commun.* **59**, 219 (1986).
- [31] V. Giovannetti, S. Lloyd, and L. Maccone, Quantum Metrology, *Phys. Rev. Lett.* **96**, 010401 (2006).
- [32] M. Li, C.-L. Zou, D. Liu, G.-P. Guo, G.-C. Guo, and X.-F. Ren, Enhanced absorption microscopy with correlated photon pairs, *Phys. Rev. A* **98**, 012121 (2018).
- [33] J. Sabines-Chesterkind, A. R. McMillan, P. A. Moreau, S. K. Josh, S. Knauer, E. Johnston, J. G. Rarity, and J. C. F. Matthews, Twin-beam sub-shot-noise raster-scanning microscope, *Opt. Express* **27**, 30810 (2019).
- [34] R. Whittaker, C. Erven, A. Neville, M. Berry, J. L. O'Brien, H. Cable, and J. C. F. Matthews, Absorption spectroscopy at the ultimate quantum limit from single-photon states, *New J. Phys.* **19**, 023013 (2017).
- [35] J. Peřina Jr., O. Haderka, V. Michálek, and M. Hamar, State reconstruction of a multimode twin beam using photodetection, *Phys. Rev. A* **87**, 022108 (2013).
- [36] A. P. Dempster, N. M. Laird, and D. B. Rubin, Maximum likelihood from incomplete data via the EM algorithm, *J. R. Statist. Soc. B* **39**, 1 (1977).
- [37] Y. Vardi and D. Lee, From image deblurring to optimal investments: Maximum likelihood solutions for positive linear inverse problems, *J. R. Statist. Soc. B* **55**, 569 (1993).
- [38] P. M. Morse and H. Feshbach, *Methods of Theoretical Physics* (McGraw-Hill, Amsterdam, 1953), Vol. 1.
- [39] J. Peřina Jr., O. Haderka, M. Hamar, and V. Michálek, Absolute detector calibration using twin beams, *Opt. Lett.* **37**, 2475 (2012).
- [40] O. Jedrkiewicz, Y. K. Jiang, E. Brambilla, A. Gatti, M. Bache, L. A. Lugiato, and P. Di Trapani, Detection of Sub-Shot-Noise Spatial Correlation in High-Gain Parametric Down-Conversion, *Phys. Rev. Lett.* **93**, 243601 (2004).
- [41] M. Bondani, A. Allevi, G. Zambra, M. G. A. Paris, and A. Andreoni, Sub-shot-noise photon-number correlation in a mesoscopic twin beam of light, *Phys. Rev. A* **76**, 013833 (2007).
- [42] J.-L. Blanchet, F. Devaux, L. Furfaro, and E. Lantz, Measurement of Sub-Shot-Noise Correlations of Spatial Fluctuations in the Photon-Counting Regime, *Phys. Rev. Lett.* **101**, 233604 (2008).
- [43] G. Brida, L. Caspani, A. Gatti, M. Genovese, A. Meda, and I. R. Berchera, Measurement of Sub-Shot-Noise Spatial Correlations Without Background Subtraction, *Phys. Rev. Lett.* **102**, 213602 (2009).
- [44] J. Peřina Jr., I. I. Arkhipov, V. Michálek, and O. Haderka, Non-classicality and entanglement criteria for bipartite optical fields characterized by quadratic detectors, *Phys. Rev. A* **96**, 043845 (2017).
- [45] J. Peřina Jr., O. Haderka, and V. Michálek, Non-classicality and entanglement criteria for bipartite optical fields characterized by quadratic detectors II: Criteria based on probabilities, *Phys. Rev. A* **102**, 043713 (2020).
- [46] I. S. Gradshteyn and I. M. Ryzhik, *Table of Integrals, Series, and Products* (Academic Press, San Diego, 2000), 6th ed.
- [47] C. T. Lee, Measure of the nonclassicality of nonclassical states, *Phys. Rev. A* **44**, R2775 (1991).
- [48] J. M. Raimond, M. Brune, and S. Haroche, Manipulating quantum entanglement with atoms and photons in a cavity, *Rev. Mod. Phys.* **73**, 565 (2001).

- [49] H. Zou, S. Zhai, J. Guo, R. Yang, and J. Gao, Preparation and measurement of tunable highpower sub-Poissonian light using twin beams, *Opt. Lett.* **31**, 1735 (2006).
- [50] M. Lamperti, A. Allevi, M. Bondani, R. Machulka, V. Michálek, O. Haderka, and J. Peřina Jr., Optimal sub-Poissonian light generation from twin beams by photon-number resolving detectors, *J. Opt. Soc. Am. B* **31**, 20 (2014).
- [51] T. S. Iskhakov, V. C. Usenko, U. L. Andersen, R. Filip, M. V. Chekhova, and G. Leuchs, Heralded source of bright multi-mode mesoscopic sub-Poissonian light, *Opt. Lett.* **41**, 2149 (2016).
- [52] J. Peřina Jr., V. Michálek, and O. Haderka, Non-classicality of optical fields as observed in photocount and photon-number distributions, *Opt. Express* **28**, 32620 (2020).
- [53] I. Straka, J. Grygar, J. Hloušek, and M. Ježek, Counting statistics of actively quenched SPADs under continuous illumination, *J. Lightwave Tech.* **38**, 4765 (2020).